Terahertz waveguides

G. Gallot,* S. P. Jamison,† R. W. McGowan,‡ and D. Grischkowsky

*School of Electrical and Computer Engineering and Center for Laser and Photonics Research,
Oklahoma State University, Stillwater, Oklahoma 74078*

Received September 1, 1999; revised manuscript received December 16, 1999

Quasi-optical techniques are used to efficiently couple freely propagating pulses of terahertz (THz) electromagnetic radiation into circular and rectangular metal waveguides. We have observed very dispersive, low-loss propagation over the frequency band from 0.65 to 3.5 THz with typical waveguide cross-section dimensions on the order of 300 μm and lengths of 25 mm. Classical waveguide theory is utilized to calculate the coupling coefficients into the modes of the waveguide for the incoming focused THz beam. It is shown that the linearly polarized incoming THz pulses significantly couple only into the TE_{11}, TE_{12}, and TM_{11} modes of the circular waveguide and the TE_{10} and TM_{12} modes of the rectangular guide. The propagation of the pulse through the guide is described as a linear superposition of the coupled propagating modes, each with a unique complex propagation vector. This picture explains in detail all the observed features of the THz pulse emerging from the waveguide. We demonstrate both theoretically and experimentally that it is possible to achieve TE_{10} single-mode coupling and propagation in a suitably sized rectangular waveguide for an incoming focused, linearly polarized THz pulse with a bandwidth covering many octaves in frequency and that overlaps more than 35 waveguide modes. Finally, to facilitate the application of these THz waveguides to THz time-domain spectroscopy of various configurations of dielectrics in the waveguide including surface layers, we present analytic results for the absorption and the dispersion of such layers. © 2000 Optical Society of America
[S0740-3224(00)01905-6]

OCIS codes: 230.7370, 300.6270, 350.4010, 320.7120, 320.5540, 310.6870.

1. INTRODUCTION

The terahertz (THz) frequency range, located midway between microwaves and visible light, presents a new frontier containing an abundance of technical applications and fundamental research problems. Consequently, THz research solutions and techniques can come from either optics or microwaves or in many cases unique combinations of both. Associated with THz investigations is the need for enabling THz technology and techniques. However, because of the developing nature of THz capability, commercial THz technology is minimal and one must rely on custom fabrication. At the present time, one-of-a-kind laboratory, optoelectronic THz transmitters and receivers provide an interim solution enabling both fundamental research and applications studies.[1,2]

One outstanding problem has been the guided-wave propagation of THz radiation and the associated efficient coupling between guided and freely propagating THz waves. Recently, efficient, broadband coupling of freely propagating pulses of THz electromagnetic radiation into circular metal waveguides has been demonstrated.[3] This work also reported the highest guided-wave performance to date, obtained with a 240-μm-diameter stainless-steel waveguide over the frequency range from 0.8 to 3.5 THz and with a power absorption coefficient of less than 1 cm^{-1}. This absorption is much less than that of coplanar and microstrip transmission lines.[3] However, for circular waveguides the undistorted propagation of picosecond THz pulses was shown not to be possible, because of the extreme dispersion near the cutoff frequencies overlapped by the pulse bandwidth covering many octaves in frequency.

A promising application of THz waveguides appears to be surface-specific frequency-dependent absorption measurements with the use of THz time-domain spectroscopy (THz-TDS).[2] From experimental measurements made on the absorption of water, we believe that for a similar polar molecule, THz-TDS has the sensitivity to characterize the absorption of nanogram quantities of samples of toxic or precious gases contained in a THz waveguide.

Here, we present a comprehensive experimental and theoretical study of the application of quasi-optical techniques to couple freely propagating pulses of THz electromagnetic radiation into both circular and rectangular metal waveguides. We observe very dispersive, low-loss propagation over the frequency band from 0.65 to 3.5 THz with frequency-dependent group velocities v_g ranging from $c/4$ to c and phase velocities v_p from $4c$ to c (where $v_p v_g = c^2$) for waveguides with typical diameters or rectangular widths of 300 μm and lengths of 25 mm. We present a complete classical waveguide theory calculation to obtain the coupling coefficients into the modes of the waveguide for the incoming focused THz beam. Even though the input spectrum overlaps the cutoff frequencies of more than 25 circular and 35 rectangular waveguide modes, the calculated coupling coefficients and the experiments show that the linearly polarized incoming THz pulses significantly couple only into the TE_{11}, TE_{12}, and TM_{11} modes of the circular waveguide and the TE_{10} and TM_{12} modes of the rectangular guide. The propagation of the THz pulse through the guide is described as a linear superposition of the coupled propagating modes, each with a unique complex propagation vector. This picture explains in detail all the observed features of the THz pulse emerging from the waveguide. We demonstrate both theoretically and experimentally that it is possible to achieve TE_{10} single-mode coupling and propagation in a suitably sized rectangular waveguide for an incoming focused, linearly polarized THz pulse with a bandwidth covering many octaves in frequency and overlapping more than 35 rectangular waveguide modes. Finally, to apply these THz waveguides to THz-TDS of dielectrics in the waveguide, we present an analytic calculation for the absorption and the dispersion of dielectric films within a waveguide.

For completeness we note that the reshaping of freely propagating THz pulses by passage through thin and thick metal slits[4,5] and dichroic metal filters[6] has been experimentally and theoretically studied. Hollow metallic waveguide transmission has been reported up to 200 GHz,[7] where the waveguides were constructed with photolithographic techniques. It should also be noted that rectangular waveguides that cover a frequency range up to 220–325 GHz are commercially available on a special-order basis, but only for small lengths up to 25 mm. Such waveguides, designated as WR-3, have typical dimensions of $850\,\mu\text{m} \times 425\,\mu\text{m}$. In comparison, the waveguide studies presented here cover the frequency range from 100 to 4000 GHz, representing a 1-order-of-magnitude increase in frequency.

The organization of this paper is as follows: First, we describe the experimental setup and the waveguide fabrication in detail, including multimode experimental results. We then present the theory of the THz-TDS optoelectronic detection of beams propagating through THz waveguides. This is followed by the theoretical and experimental demonstration that a THz beam can be coupled into a single mode and propagate in a suitably sized rectangular waveguide. We conclude with a theoretical study of some applications made possible by the use of a single-mode propagation, in the domain of spectroscopic measurements of waveguides with thin films. This is followed by a complete description in Appendixes A and B of the microwave theory used to obtain our coupling coefficients and complex propagation vectors. The new results pertaining to the THz waveguide and the THz-TDS problem constitute the theory section in the main body of the manuscript.

2. EXPERIMENTAL SETUP

The experimental setup for broadband THz waveguides, shown in Fig. 1, consists of an optoelectronic transmitter and receiver along with beam-shaping and beam-steering optics. A detailed description of the entire system has been previously published.[1,2] The picosecond THz pulses are generated as follows: 40-fs optical pulses at 820 nm from a KLM Ti:sapphire laser are focused onto the edge of the positive line of a coplanar strip line on semi-insulating GaAs, which is dc biased at 70 V. The optical pulse creates an electron–hole plasma, and the subsequent acceleration of the carriers generates a near-single-cycle electromagnetic pulse of THz radiation that is linearly polarized along the direction of the bias field. In the standard THz-TDS setup, the sample is placed at the THz beam waist at the confocal position between the two parabolic reflectors. The THz beam system has symmetric confocal optics with respect to the center line of the system between the transmitter and the receiver. This situation gives a unity, frequency-independent, power coupling efficiency between the transmitter and the receiver (see Eq. (2.16), Ref. 8). The transmitting antenna is at the focus of the silicon lens, which collimates the frequency-independent far-field pattern of the antenna into an approximately Gaussian beam with a 1/*e* beam waist diameter of 5 mm and with a plane-wave phase front. This is beam waist W1. This beam waist is in turn in the focal plane of the transmitter paraboloidal mirror, which focuses the THz beam to the second beam waist W2 with beam diameters proportional to wavelength and with plane-wave phase fronts. In the standard system, the THz optical train is identical (but reversed) from this point on to the receiver. For the waveguide experiments, an additional silicon lens is placed at the beam waist W2, thereby producing a third frequency-independent beam waist W3 with a 1/*e* amplitude waist diameter of 200 μm and a plane-wave phase front. This third beam waist overlaps the waveguide entrance face. The output face of the waveguide is again in the focal plane of an identical silicon lens with identical but reversed optics to the receiver. In the absence of the waveguide and with the two identical silicon focusing lenses moved so that their beam waists overlap, the entire system is again confocal and gives a frequency-independent, power coupling efficiency of unity between the THz transmitter and receiver. With the waveguide in place, the total coupling efficiency between the transmitter and the receiver is determined by the product of the coupling efficiency of the incoming THz beam into the waveguide, the transmission factor of the waveguide, and the coupling efficiency of the output beam into the THz receiver. Because the input and output faces of the waveguide are in the focal planes (beam waist) of the identical focusing lenses, the coupling efficiency of the incoming THz beam is identical to the coupling efficiency of the output beam into the THz receiver. This coupling efficiency is determined by evaluating the overlap integral between the THz beam waist and the modes of the waveguide (see Eq. (2.1), Ref. 8).

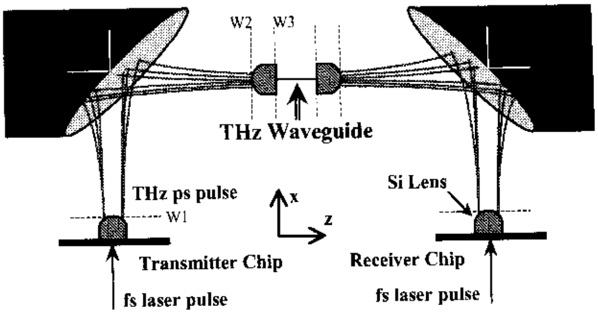

Fig. 1. Optoelectronic THz-TDS system incorporating quasi-optical coupling to the THz waveguide. The generated THz pulse is linearly polarized in the plane of the figure and along the *X* axis at the waveguide entrance face.

The transmitted pulse is focused onto a polarization-sensitive, 10-μm dipole antenna on ion-implanted silicon-on-sapphire, which is photoconductively switched by a second beam of 40-fs optical pulses, generating a dc current that is proportional to the instantaneous electric field of the propagated THz pulse. By scanning the relative delay between the detected THz pulse and the gating optical pulse, one obtains the entire time-dependent THz pulse, including both field and phase information.

All of the waveguides used in this experiment were fabricated in our laboratory by using commercially available stock. The stainless-steel circular waveguide was made from the most precise metal tube available, a stainless-steel hypodermic needle. This long guide was 25 gauge and was 24 mm long with a 240-μm diameter. The short guide was also 25 gauge but had a measured 280-μm diameter and a length of 4 mm. Although the hypodermic needles are the best commercial tubes available, they have significant inconsistency in inner-diameter dimensions and circular precision. To ensure no deformation of the tubes during the cutting process, we encapsulated the tube in hard mounting wax on a hot plate. Once encapsulated, the tube was cut on a wire saw with low cutting pressure. The mounting wax was removed by ultrasounding in acetone, and the edges were carefully deburred. This method is extremely important for softer waveguide metals such as copper and brass. Compared with stainless steel, which has a conductivity of $1.1 \times 10^6\,\Omega^{-1}\,\mathrm{m}^{-1}$, much longer waveguides of high-conductivity metals could be used, for example, copper and brass. Copper has a conductivity 36 times larger than that of stainless steel, giving an absorption coefficient six times smaller for Cu than for stainless steel. Brass is also a good choice, with a conductivity slightly less than that of copper. However, for copper we could not obtain circular tubing without significant ellipticity and cross-section variations with length. Consequently, the complicated experimental results for copper guides are not presented here.

The rectangular waveguides discussed here have been fabricated by cutting grooves in brass plates. With the use of a 250-μm jeweler's saw blade, a precise groove is cut on a 25-mm-square, 6-mm-thick brass plate. Another brass plate is tightly connected to the grooved plate to complete the waveguide. The entrance and exit sides of the guide are carefully milled to obtain high-precision flat and burr-free entrance and exit faces. To study the influence of the waveguide dimension on the relative coupling efficiencies, we cut several waveguides of different size on the same 25-mm-long plate.

3. EXPERIMENTAL RESULTS FROM CIRCULAR WAVEGUIDES

The first experimental results were obtained with circular stainless-steel waveguides.[3] A reference pulse is obtained by removing the waveguide and moving the two silicon lenses to near contact with a 300-μm-diameter aperture placed between them at their common focus W3. Figure 2(a) shows the reference THz pulse, and Fig. 2(b) shows that the useful amplitude spectrum extends from 0.1 to 4 THz. Figure 3(a) shows the measured transmitted pulse through the 24-mm-long, 240-μm-diameter stainless-steel circular waveguide. The incoming coupled pulse, which has a duration of approximately 1 ps, has been stretched to approximately 70 ps, with the high frequencies arriving earlier in time, corresponding to negative chirp. The stretching and the consequent chirping of the transmitted pulse of Fig. 3(a), compared with the input pulse of Fig. 2(a), is due to the strong group-velocity dispersion of the waveguide. The waveguide acts as a dispersive delay line, where the lower frequencies travel more slowly than the higher frequencies. Figure 3(b) shows the corresponding amplitude spectrum for the waveguide. Note the sharp cutoff at 0.76 THz, which compares well with the theoretically calculated cutoff of the lowest-order waveguide mode TE_{11} of 0.76 THz (see Appendix B). The spectrum presents unusual oscillations starting at approximately 1.7 THz. As demonstrated in the theoretical section, these oscillations are due to multimode propagation through the waveguide.

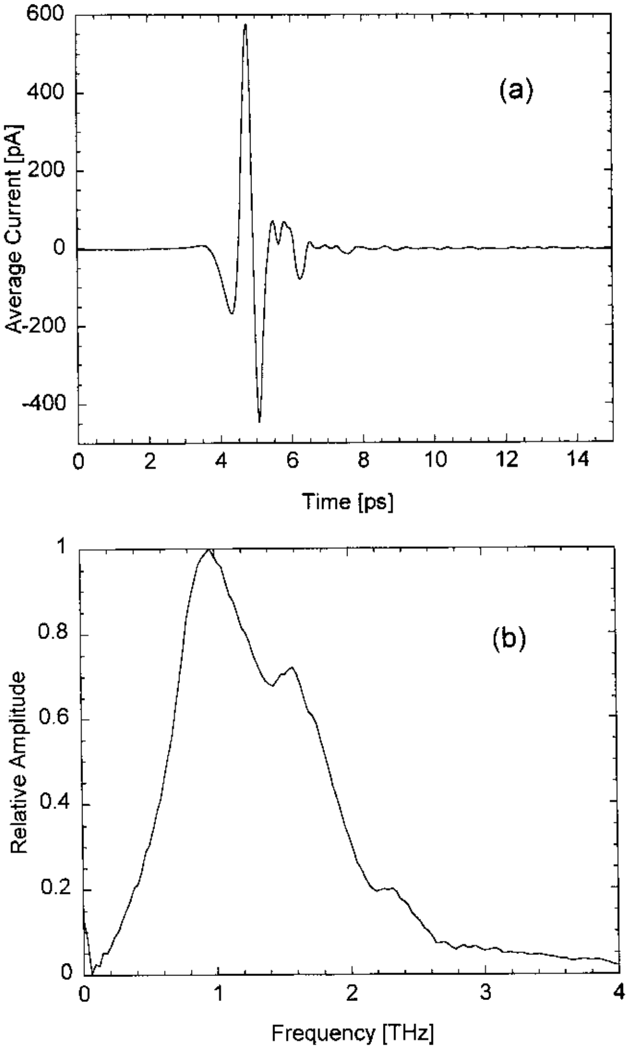

Fig. 2. (a) Measured reference THz pulse and (b) relative amplitude spectrum of the reference pulse. The small oscillations apparent in (a) at approximately 6 ps are due to reflections between the confocal silicon lenses.

Experiments have been performed with several other guides, including brass and nickel circular waveguides. Because of changes in alignment, the reference pulse varies between experiments, although the general features of Fig. 2(a) remain unaltered. Figure 4 shows the measured THz (a) pulse and (b) spectrum transmitted through a 25-mm-long, 280-μm-diameter brass circular waveguide. A sharp cutoff at 0.67 THz is also observed in the brass guide, while for a 280-μm guide the cutoff is calculated to be 0.65 THz.

The qualitative results obtained for the stainless-steel (Fig. 3) and brass (Fig. 4) circular waveguides are quite different. For similar input pulses, the maximum amplitude of the pulse transmitted through the brass waveguide is twice that from the stainless-steel waveguide. The temporal stretches, at $1/e$, for the stainless-steel and brass waveguides, respectively, are 20 and 40 ps. The pulse emerging from the brass waveguide is therefore twice as long as the one exiting from the stainless-steel waveguide. These results demonstrate the significantly reduced loss of the brass waveguide and are in good agreement with our theoretical simulations. Precise quantitative results were not obtained because the shape of the tubes is not constant and is not well defined. These imperfections lead to perturbations of the waveguide modes and rotation of the THz polarization during propagation.

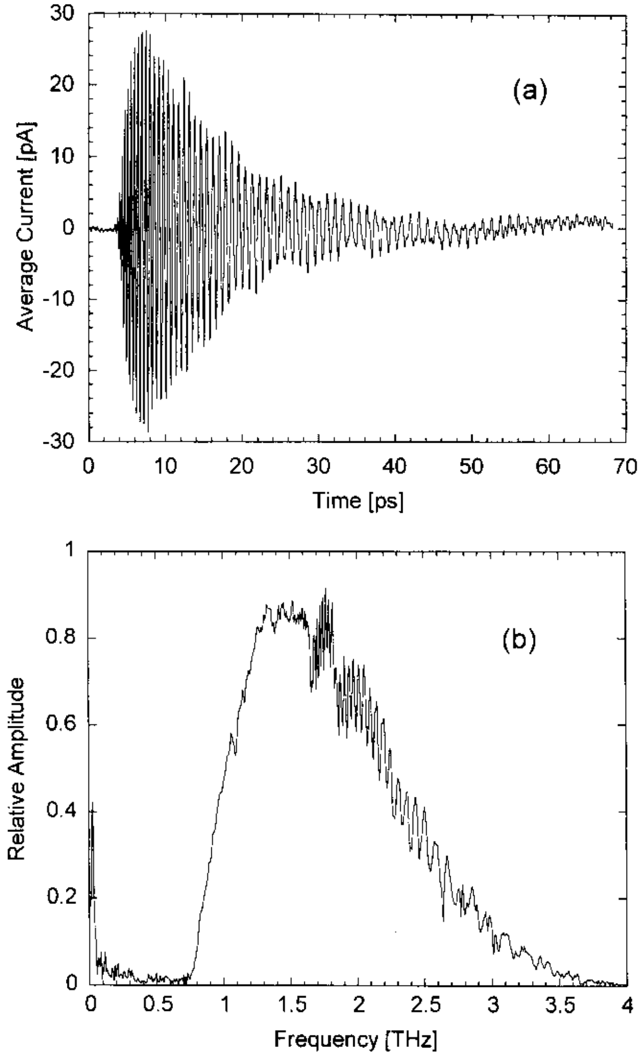

Fig. 3. (a) Measured THz pulse transmitted through a 24-mm-long, 240-μm-diameter stainless-steel waveguide. The input pulse is shown in Fig. 2(a). (b) Amplitude spectrum of the measured transmitted pulse.

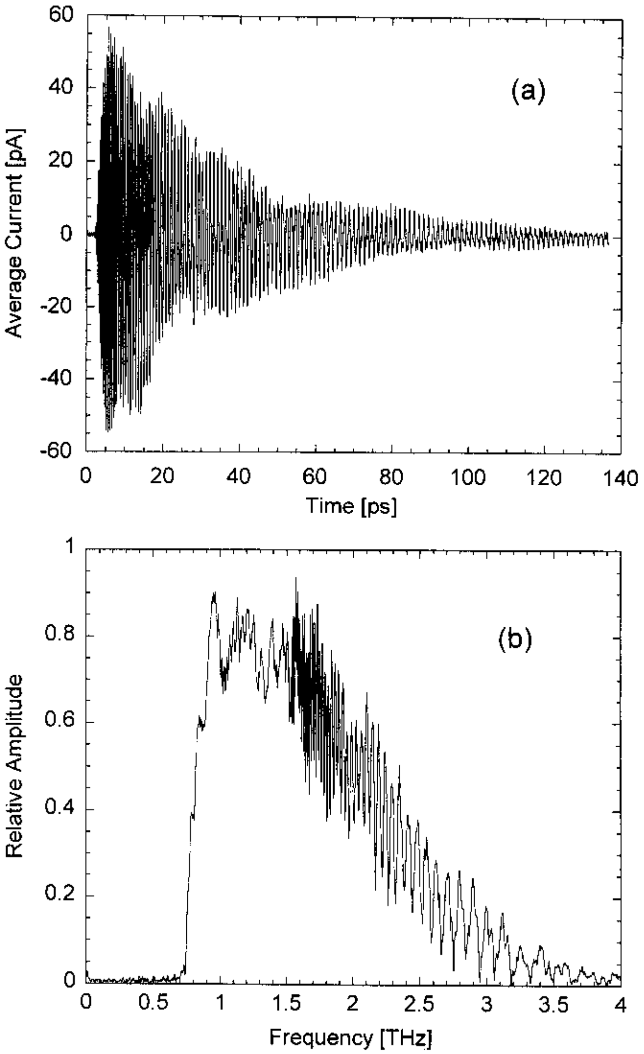

Fig. 4. (a) Measured THz pulse transmitted through a 25-mm-long, 280-μm-diameter brass waveguide. The input has a duration of approximately 1 ps. (b) Amplitude spectrum of the measured transmitted pulse.

4. INTRODUCTION TO THEORY

To study the behavior and the propagation of a subpicosecond pulse of THz radiation in a metallic waveguide, the modern and current approach would be to directly solve Maxwell's equations by finite-difference time-domain numerical simulation.[9] In such an approach, the electric and magnetic fields are calculated through an iterative application of the boundary conditions. After propagation through the guide, the temporal pulse and spectrum are obtained, but what happens in the guide is not intuitively clear. Quasi-optical methods combined with microwave theory are an analytic alternative whereby the incoming wave of THz radiation at the entrance to the waveguide is expanded as a sum of the stationary field patterns of the modes of the waveguide. The waveguide modes have been studied for many years in microwave technology, so that the theory is well established (see Appendix A). In the case of optoelectronically generated, subpicosecond pulses of THz radiation, the large bandwidth makes new phenomena appear, such as interference between modes and exceptionally large dispersion.

5. COHERENT POLARIZED TERAHERTZ ELECTRIC FIELD DETECTION

We consider now the coherent detection of the THz radiation emerging from the waveguide.[1,2] The electric field $\mathbf{E}_t$ at the output of the guide can be expressed in terms of its components with respect to the X and Y axes as

$$\mathbf{E}_t(x, y, z) = E_x(x, y, z)\hat{e}_x + E_y(x, y, z)\hat{e}_y. \qquad (1)$$

In general, for any THz receiver with $\mathbf{R}(x, y, z, \omega)$ designating the beam pattern that is collected with unity coupling efficiency, the measured output field of the waveguide would be given by the overlap integral of $\mathbf{E}_t$ with $\mathbf{R}(x, y, z, \omega)$.[8] Our receiver is optically identical to the transmitter; it is linearly polarized along the X axis, and the accepted beam profile at the focal plane (located at the output face of the waveguide) of the output silicon lens is the same as that of the incoming THz beam to the waveguide at the beam waist, namely, a Gaussian profile $E_g(x, y)$ with a frequency-independent $1/e$ amplitude diameter of 200 μm and a planar phase front. Consequently, $\mathbf{R}(x, y, z, \omega) = E_g(x, y)\hat{e}_x$. Using the normal-mode expansion of Eq. (A6) from Appendix A, one obtains the expression for the detected signal E_d in terms of normal modes designated by the subscript p:

$$E_d(\omega, t) = \sum_p A_p X_p t_{\mathrm{out}} \exp[i\omega t - \gamma_p(\omega) z], \qquad (2)$$

where

$$X_p = \iint_S \mathbf{E}_{tp} \cdot E_g \hat{e}_x \mathrm{d}S = \iint_S E_{p,x} E_g \mathrm{d}S \qquad (3)$$

and t_{out} is the transmission factor out of the waveguide given in Eqs. (A10). The integration is over the output face S of the waveguide. Because of this integral nature of the detected field, our receiver cannot detect modes with zero overlap integral; odd modes are not detectable. The detected signal $E_d(\omega, t)$ is expressed as the summation of sinusoidal functions $\exp[i\omega t - i\beta_p(\omega)z]$, which is responsible for additional oscillations in the temporal domain and for interference fringes in the spectral domain. For instance, the power spectrum of the signal detected in the presence of two modes is

$$|E_d|^2 = c_1(\omega)\{1 + c_2(\omega)\cos[\beta_2(\omega) - \beta_1(\omega)]z\}, \qquad (4)$$

where c_1 and c_2 are constants depending on the particular modes. Thus, as a result of the strong frequency dependence of the propagation constants, interference appears where the two modes overlap the same frequency range, that is to say, for frequencies higher than the highest cutoff frequency of the two modes. The interference described in Eq. (4) for the power spectrum is at first surprising, since the modes are orthogonal and linearly independent; however, for a receiver such as a bolometer, which detects the power rather than the electric field, there will be no interference in the power spectra.

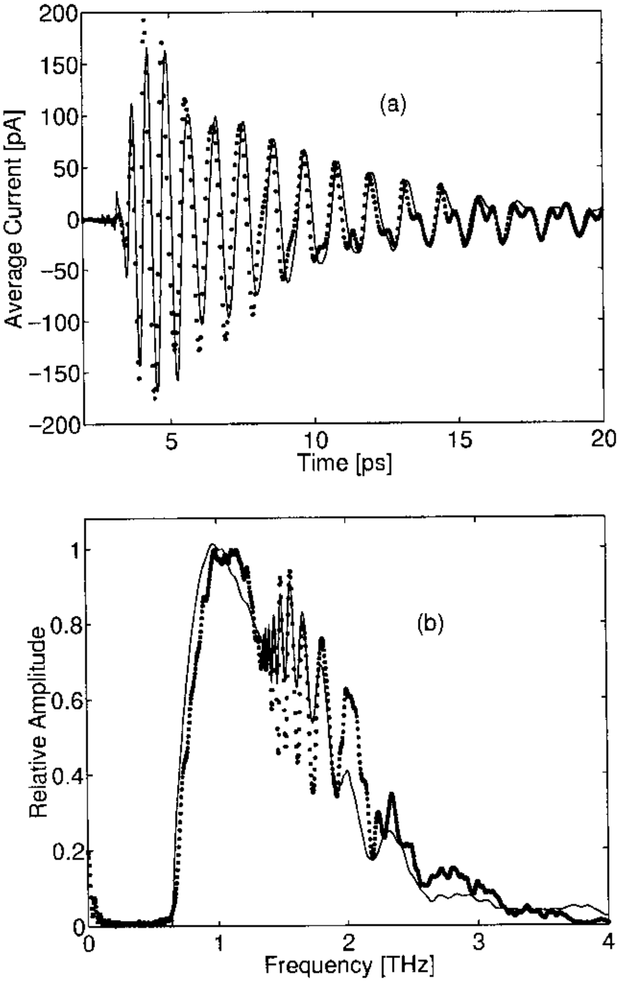

Fig. 5. (a) Measured THz pulse (dots) transmitted through a 4-mm-long, 280-μm-diameter stainless-steel waveguide and (b) amplitude spectrum (dots) of the measured transmitted pulse [Fig. 5(a)]. The solid curves are the theoretical predictions.

Using Eqs. (2) and (A6), we compare the experimental (dots) and theoretical (solid curves) pulse shape and spectrum of a THz pulse transmitted through a 4-mm-long, 280-μm-diameter stainless-steel waveguide in Figs. 5(a) and 5(b), respectively. For the best fit the theory used a waveguide diameter of 270 μm, a beam diameter of 160 μm, and the spectrum of the reference pulse, and it evaluated the coupling coefficients according to Appendix A. Analysis of this comparison shows that experimentally, the amplitude of the TM_{11} mode was approximately twice that predicted. We ascribe this discrepancy to waveguide imperfection. Under these circumstances we consider the agreement between theory and experiment to be quite satisfactory.

6. SINGLE-MODE PROPAGATION

In general, a single-mode, single-conductor waveguide capable of propagating a subpicosecond THz pulse is not possible, because the pulse bandwidth overlaps many octaves in frequency. However, this situation does not preclude the pulse propagating in a single mode of the waveguide if coupling to only one mode can be performed.

The lower cutoff frequencies of the modes in a waveguide are approximately distributed in frequency by octave. If the bandwidth of the incoming signal is narrow enough (less than a factor of 2 in the frequency range), it is possible to choose the dimensions of the guide so that the bandwidth lies between the lowest cutoff frequency and the next-higher-order mode. But for a wider bandwidth of many octaves, which is the case for optoelectronically generated, subpicosecond pulses of THz radiation, the cutoff frequencies of many modes will be in the frequency range of the signal. Consequently, many higher-order modes can be excited. However, the relative amplitudes of the coupling coefficients to these modes are sensitive to the polarization, the shape, and the phase front of the incoming beam relative to the geometry of the guide. By changing the dimensions of the guide, the shape, or the polarization of the beam, one can favor the coupling into select modes.

We performed numerical simulations of the mode projection of our incoming Gaussian beam coupled into different waveguides. The mode projection is determined by decomposing the input field into transmitted and reflected waveguide modes. The coefficients A_p and B_p for the modes designated by the index p are defined by Eqs. (A7) from Appendix A and represent the transmitted and reflected mode amplitudes, respectively. These coefficients are real because we consider coupling at the beam waist, for which the field is planar. The relative transmitted power P_p into specific waveguide modes is given by

$$\frac{P_p(\omega)}{P_{\text{incident}}} = G\frac{Z_p(\omega)}{Z_0}A_p^2(\omega), \tag{5}$$

where we refer to the fraction of the energy incident on the aperture of the waveguide compared with the total incident energy as the geometric transmission, denoted G. The impedance of the medium outside the waveguide is denoted Z_0, and $Z_p(\omega)$ is the waveguide impedance of the mode, referring to either Z_p^{TE} or Z_p^{TM}, defined in Eqs. (A4) from Appendix A. The coupling efficiency of Eq. (5) can be separated into frequency-dependent and frequency-independent terms by introducing a power transmission coefficient $T(\omega)$ and the frequency-independent mode projection $(A_p + B_p)$ at the guide entrance calculated in Eqs. (A7). Then

$$\frac{P_p(\omega)}{P_{\text{incident}}} = G(A_p + B_p)^2T(\omega),$$

$$T(\omega) = \frac{Z_p(\omega)}{Z_0}\left(\frac{A_p}{A_p + B_p}\right)^2 = \frac{4Z_0Z_p(\omega)}{[Z_0 + Z_p(\omega)]^2}. \tag{6}$$

Figure 6 shows the calculated mode projection squared $(A_p + B_p)^2$ of the dominant five modes TE_{11}, TE_{12}, TE_{13}, TM_{11}, and TM_{12} for a circular guide as a function of the guide diameter. The solid curve labeled "sum" is the normalized sum of the squares of the mode projections in the above five modes, where the normalized sum of the squares of the projections for all the modes of the waveguide is equal to unity. It is found that TE_{11} remains the dominant mode over a wide range of guide diameters, with a maximum mode projection occurring for a diameter of 200 μm, equal to that of the incoming beam. Even for this optimal combination, the maximum projection for the TE_{11} mode remains below 90%. The main reason for this continued multimode coupling is that the linear polarization of the incoming beam is not fully compatible with the boundary conditions of the circular waveguide, as can be seen from an inspection of the field pattern of the TE_{11} cylindrical mode shown below in Fig. 12 in Appendix B. This can also be observed in Fig. 3(b), where the amplitude spectrum transmitted through a 24-mm-long, 240-μm-diameter waveguide shows an obvious interference pattern, in good agreement with the mode projections presented in Fig. 6.

In contrast to the circular waveguides, inspection of the field pattern of the TE_{10} mode of the rectangular waveguide, displayed in Appendix B as Fig. 10, shows that this mode is fully compatible with a linearly polarized incoming wave. Figure 7 shows the mode projection squared $(A_p + B_p)^2$ of the dominant four modes TE_{10}, TE_{30}, TE_{32}, and TM_{12} of a rectangular guide as a function of the guide dimensions for the linearly polarized incoming plane-wave beam with a 1/*e* waist diameter of 200 μm. In Fig. 7(a) the dimension b along the polarization of the beam is kept constant, equal to 280 μm, and the dimension a varies from 50 to 600 μm. The mode projection of the dominant mode TE_{10} presents a relatively broad maximum, remaining below 80%, and therefore the propagation is not single mode. However, in contrast to circular waveguides, the second dimension of the rectangular guide remains as a variable. Taking the best value for the dimension a, we vary the dimension b, as shown in Fig. 7(b), and observe that the TE_{10} mode projection can approach unity if b is chosen small enough. For this condition the beam propagates through the guide as a single TE_{10} mode. Of course, the limitation on b is the fraction of the incident power transmitted through the rectangular aperture of the waveguide, G. A compromise between the best dominant mode projection and the maximum transmitted power needs to be found. For instance, with a rectangular guide of dimensions 280 μm × 130 μm, G

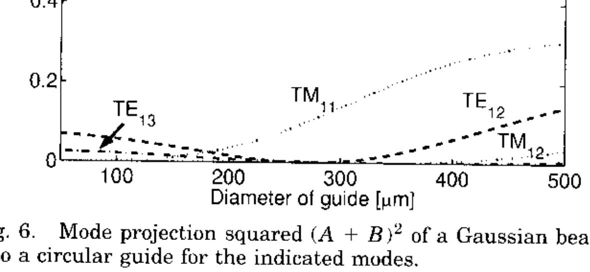

Fig. 6. Mode projection squared $(A + B)^2$ of a Gaussian beam into a circular guide for the indicated modes.

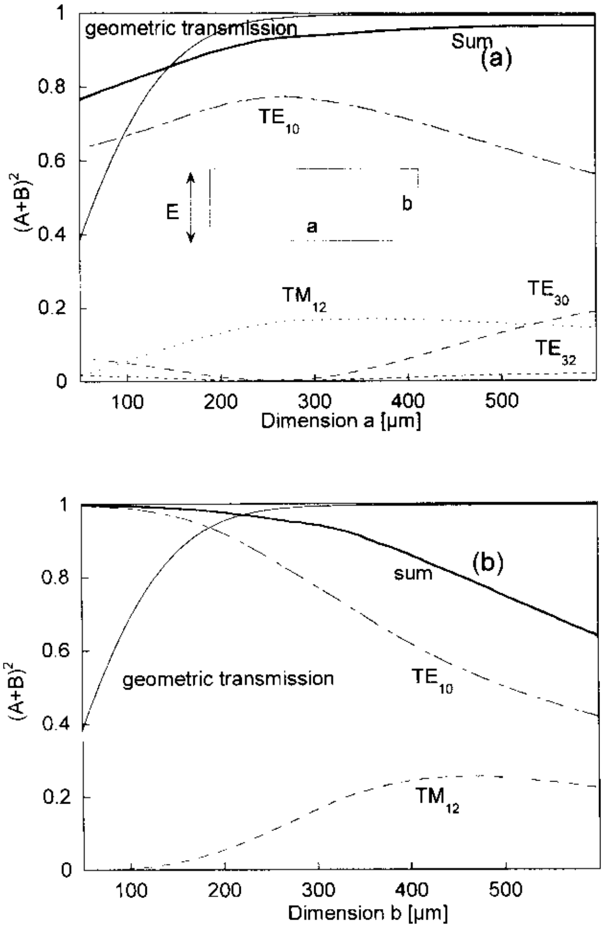

Fig. 7. Mode projection squared $(A + B)^2$ of a Gaussian beam with the indicated polarization into a rectangular guide of dimensions $a \times b$ for the modes TE_{10}, TE_{30}, TE_{32}, and TM_{12}. (a) The dimension a of the guide varies from 50 to 600 μm with $b = 300\,\mu$m, and (b) the dimension b varies from 50 to 600 μm with $a = 280\,\mu$m.

is more than 80%, and the mode projection $(A_p + B_p)^2$ of the beam is more than 98% into the dominant mode TE_{10}. For any given beam size, it is possible to design a rectangular waveguide with very high coupling efficiency into the dominant mode and simultaneously a good geometric transmission of the aperture, as the relative mode projections are due solely to the relative dimensions of the beam waist and the waveguide. Because a change in the dimensions of the guide affects the cutoff frequency, the final size of the waveguide must also take into account the bandwidth of the THz beam.

We can now apply these principles to experimentally test for the single propagating TE_{10} mode. The relative amplitude spectra of THz pulses propagating through three different rectangular waveguides are presented in Fig. 8. The brass waveguides have the following respective dimensions ($a \times b$): (a) $250\,\mu\text{m} \times 800\,\mu\text{m}$, (b) $250\,\mu\text{m} \times 250\,\mu\text{m}$, and (c) $250\,\mu\text{m} \times 125\,\mu\text{m}$. The calculated cutoff for the lowest-order mode TE_{10} is 0.6 THz for the waveguide of Fig. 8(c). For this waveguide the modal characteristics are shown in Figs. 10 and 11 in Appendix B. The transmitted spectrum presented in Fig. 8(a) shows a dramatic interference pattern corresponding to the superposition of several modes during the propagation. As shown above in Fig. 7, the reduction of the dimension b of the waveguide leads to reduction of the amplitude of oscillation [Fig. 8(b)] and even to a complete disappearance of the oscillations within our signal-to-noise ratio in Fig. 8(c). The propagation of the THz pulse through this waveguide with dimensions $250\,\mu\text{m} \times 125\,\mu\text{m}$ is effectively a single-mode propagation. Qualitatively, the agreement between the amplitude of the oscillation found in the experimental spectrum of Fig. 8 and the amplitude obtained with the mode projections is excellent. The oscillations in Figs. 8(a), 8(b),

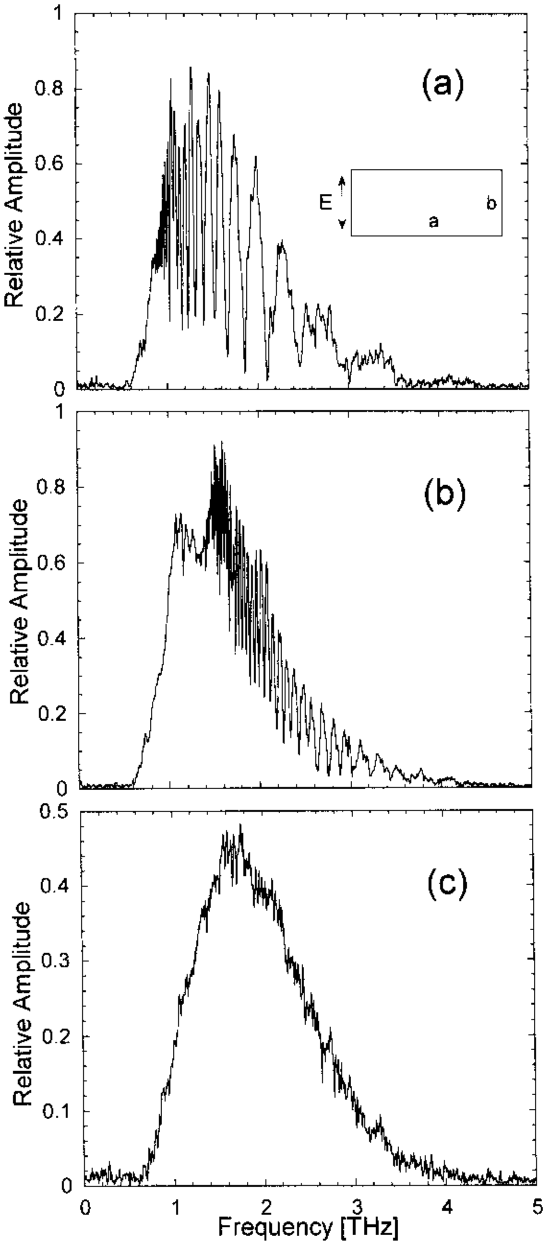

Fig. 8. Relative amplitude spectra of a subpicosecond pulse of THz radiation after propagation through a rectangular brass waveguide with different sizes of the guide. The dimensions of the guides ($a \times b$) are (a) $250\,\mu\text{m} \times 800\,\mu\text{m}$, (b) $250\,\mu\text{m} \times 250\,\mu\text{m}$, and (c) $250\,\mu\text{m} \times 125\,\mu\text{m}$. The length of the guides is 25 mm.

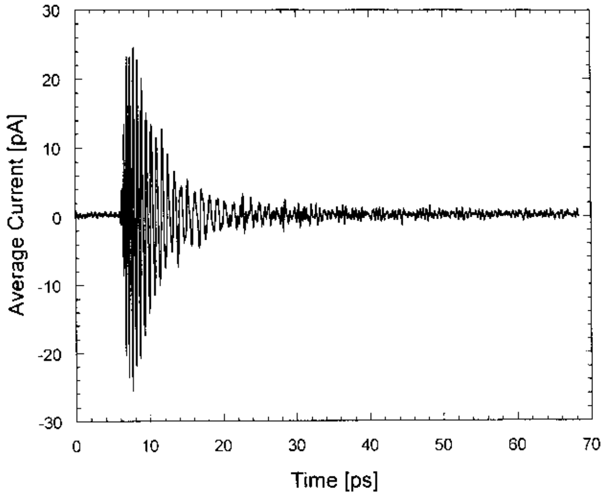

Fig. 9. Measured THz pulse transmitted through a 25-mm-long, 250-μm × 125-μm rectangular brass waveguide.

and 8(c) present modulations of 0.64, 0.45, and 0.06, respectively, compared with the theoretical modulations of 0.67, 0.52, and 0.07, respectively. Here, the modulation is defined as the ratio of the total amplitude of the oscillation to the average value of the spectrum.

Figure 9 presents the measured THz pulse transmitted through the 25-mm-long, 250-μm × 125-μm waveguide corresponding to the spectrum of Fig. 8(c). The transmitted pulse shows regular oscillations with some irregular structure on the trailing edge of the pulse that is due to water vapor in the path of the THz beam. Although the pulse has been significantly broadened by the group-velocity dispersion of the TE_{10} mode, the resulting 13-ps, 1/*e* pulse width is significantly less than the corresponding 40-ps, 1/*e* pulse width for the brass circular guide as shown in Fig. 4. This is due to the difference between single-mode and multimode propagation in the waveguides and to the different dimensions.

7. WAVEGUIDE THz-TDS

We have demonstrated, in both theory and experiment, the feasibility of single-mode excitation of a rectangular THz waveguide. We now present the theory that enables the application of this new THz technology to THz-TDS (Ref. 2) spectroscopic measurements of dielectrics in the waveguide, which include thin-film and gas measurements. The developed theory obtains equations for the measurement of the absorption and the dispersion of the dielectric media.

We now consider the case of waveguides partially filled with a thin dielectric layer. In Appendix C it is shown that the absorption coefficient in a layer within the waveguide, $\alpha_{g,l}$, is related to that of the bulk dielectric, α_l, by

$$\alpha_{g,l} = f\alpha_l \frac{v_l}{v_g}, \tag{7}$$

where the filling factor *f* is defined as the ratio of the energy in the layer to the total energy within the guide. This expression for the absorption coefficient is general and applies to any distribution of dielectric in the guide. In most cases the group velocity in the layer material can be approximate to the phase velocity c/n_l, where n_l is the refractive index of the layer material. For a thin layer, the group velocity of the guide is approximately that of the air-filled waveguide. Using Eqs. (A8), one obtains the absorption by propagation through the waveguide with no conductive loss as

$$\alpha_{g,l} = f\alpha_l \frac{1}{n_l[1 - (\lambda/\lambda_c)^2]^{1/2}}. \tag{8}$$

The absorption depends on the wavelength, increasing as the wavelength approaches the cutoff wavelength. This enhancement of the bulk absorption of the layer can be understood by the behavior of the propagating fields near the cutoff. In a geometrical picture, the waves in the guide are reflected by the sidewalls of the metal waveguide. The closer the wavelength is to the cutoff, the bigger the angle is between the wave and the wall. Consequently, the effective length of travel is then increased by the zigzag path, intensifying the effective absorption in the guide.[10]

To obtain the total loss, we need to add the conductive loss. For a thin dielectric layer, for which the group velocity is approximately equal to that of an empty guide, the conductive losses are unchanged by the presence of the dielectric layer. The total loss is then given by

$$\alpha_T = \alpha_{g,l} + \alpha_{\text{TE}} \ (\text{or } \alpha_{\text{TM}}), \tag{9}$$

where $\alpha_{g,l}$ is given by our Eq. (8) and α_{TE} and α_{TM} are given by Marcuvitz[11] (Eq. 9, page 60, and Eq. 4, page 57, for a rectangular guide and Eq. 25, page 70, and Eq. 21, page 67, for a circular guide).

As an example for the rectangular waveguide, we can apply the filling factor of the mode TE_{10} to obtain the absorption coefficient in the guide that is due to an absorbent layer. The filling factors for rectangular and circular waveguides with a thin dielectric layer adjacent to their surfaces have been evaluated and are given in Appendix C. By combining Eqs. (8) and (C10), we obtain

$$\alpha_{10} = \frac{1}{n_l^3} \frac{\alpha_l}{[1 - (\lambda_0/\lambda_c)^2]^{1/2}} \frac{\Delta l}{b} + \alpha_{\text{TE}} \ (\text{or } \alpha_{\text{TM}}). \tag{10}$$

The first part is due to the absorption from the layer itself, and the second part is due to the conductive loss in the metal of the guide.

For a thin layer in the waveguide of length *L*, the detected amplitude spectrum $E_l(\omega)$ is proportional to $\exp(-\alpha_T L)$, whereas the reference amplitude spectrum $E_{\text{empty}}(\omega)$ for the air-filled waveguide is proportional to $\exp[-\alpha_{\text{TE}}(\text{or } \alpha_{\text{TM}})L]$. The ratio of the amplitude spectrum of the waveguide with the layer to the reference amplitude spectrum gives $\exp(-\alpha_{g,l}L)$. Finally, with the use of Eq. (8), the absorption coefficient of the layer α_l is obtained from the ratio of the two amplitude spectra E_{empty} and E_l by

$$\alpha_l = -\frac{1}{fL}\left[1 - \left(\frac{\lambda_0}{\lambda_c}\right)^2\right]^{1/2} \ln\left|\frac{E_l(\omega)}{E_{\text{empty}}(\omega)}\right|. \tag{11}$$

A. Measurement of the Absorption from a Thin Layer in a Waveguide

The above result can be compared with traditional methods, where the layer covers a mirror and where the change of absorption from the layer is detected. In this case, with a layer of the same thickness, the amplitude absorption is given by $\exp(-\alpha_l \times 2\Delta l)$, where the factor 2 is due to the fact that the layer is traveled through twice. If now we take a guide of length L, the absorption is then $\exp(-\alpha_{10}L)$. For a wavelength much smaller than the wavelength cutoff, the ratio of the effective lengths is given by

$$\Gamma_{\text{wg}} = \frac{\alpha_{10}L}{\alpha_l \times 2\Delta l} = \frac{1}{2n_l^3}\frac{L}{b}. \tag{12}$$

This ratio is very sensitive to the index of the layer. For an index close to unity, Γ_{wg} may be much bigger than 1. For example, for a waveguide where $L = 100$ mm and $b = 125\ \mu$m and for a layer with an index $n_l = 2$, Γ_{wg} is equal to 50. It is possible in this waveguide case to measure absorption with samples 50 times less absorbent than is possible with traditional single-layer reflection. On the contrary, for a high index, Γ_{wg} is small, and this technique is not as effective. However, for the study of single molecular layers or chains with $n_l \approx 1$ this technique can yield extremely large sensitivity enhancements.

B. Determining the Dielectric Constant of a Thin Dielectric Layer in the Waveguide

Through comparison of the phase of the electric field, in both an air-filled guide and one in which a thin dielectric layer is present, it is possible to determine the dielectric constant of the layer. We consider a rectangular waveguide with a thin layer adjacent to the waveguide surface and a polarization of the THz beam inside the waveguide orthogonal to the surface of the layer. The phase of the electric field is determined by the propagation constant of the guide, such that $E(\omega) = |E(\omega)|\exp(-i\beta L)$. For a nonabsorbing dielectric, we can then compare a sample and a reference spectrum to obtain

$$\arg\left(\frac{E_l}{E_{\text{empty}}}\right) = (\beta_{\text{empty}} - \beta_l)L = \left(\frac{2\pi}{\lambda_{g,\text{empty}}} - \frac{2\pi}{\lambda_{g,l}}\right)L, \tag{13}$$

where arg represents the argument (angle) of the complex ratio. Marcuvitz has presented the following approximate expression for $\lambda_{g,l}$ for the dominant (approximately TE_{10}) mode[11]:

$$\lambda_{g,l} \approx \frac{\lambda_0}{\left[\dfrac{1}{1 - \dfrac{\Delta l}{b}\left(1 - \dfrac{1}{\epsilon_l}\right)} - \left(\dfrac{\lambda_0}{2a}\right)^2\right]^{1/2}}, \tag{14}$$

where ϵ_l is the relative dielectric constant of the layer, a and b are the dimensions of the rectangular guide, and Δl is the dielectric thickness. With this result an expansion in terms of the dielectric thickness leads to the first-order expression

$$\beta_{\text{empty}} - \beta_l = \frac{\pi(1/\epsilon_l - 1)}{b\lambda_0\left[1 - \left(\dfrac{\lambda_0}{2a}\right)^2\right]^{1/2}}\Delta l. \tag{15}$$

This result, together with Eq. (13), leads to an expression for the relative dielectric constant of the layer:

$$\epsilon_l = \frac{1}{1 + \arg\left[\dfrac{E_l(\omega)}{E_{\text{empty}}(\omega)}\right]\dfrac{\lambda_0 b}{\pi L \Delta l}\left[1 - \left(\dfrac{\lambda_0}{2a}\right)^2\right]^{1/2}}. \tag{16}$$

8. CONCLUSIONS

We have demonstrated the efficacy of quasi-optical techniques to efficiently couple freely propagating pulses of THz radiation into submillimeter circular and rectangular waveguides with typical diameters and edge dimensions of 300 μm and with lengths of 25 mm. We observed low-loss, very dispersive propagation through these waveguides over the frequency band from 0.65 to 3.5 THz with frequency-dependent group velocities v_g ranging from $c/4$ to c and phase velocities v_p from $4c$ to c. The low loss, inversely proportional to the square root of the conductivity, would enable propagation lengths much longer than the previous 25-mm lengths to be demonstrated. Here, the experimental limitation is the availability of longer lengths of precision metal tubing to be used as waveguides.

Even though our input spectrum overlaps the cutoff frequencies of more than 25 waveguide modes, the linearly polarized incoming THz pulses significantly couple only into five modes for the circular waveguides and four modes for the rectangular waveguides. Using classical waveguide theory, we obtain the coupling coefficients into the modes of the waveguides for the incoming focused THz beam, where the propagation of the THz pulse through the waveguide is described as a linear superposition of the coupled propagating modes, each with a unique complex propagation vector. We demonstrate that this superposition of the propagating modes explains in detail all of the observed features of the THz pulse emerging from the waveguide.

Through our understanding of the coupling of the incoming linearly polarized, focused THz pulse with a plane-wave phase front to the waveguide modes, we show that it is possible to design a rectangular waveguide for which the THz pulse couples to only a single mode of the waveguide. We have experimentally demonstrated this conclusion by observing single-mode propagation over the frequency range from 0.7 to 4 THz for an optimal 250-μm × 125-μm rectangular brass waveguide 25 mm long. These results are significant in that they enable THz pulse propagation in the waveguide with a single-valued, analytic propagation vector.

Such single-mode propagation makes possible the application of waveguide THz time-domain spectroscopy (THz-TDS). To facilitate these applications, we have developed a waveguide theory for thin-film measurements and have shown that an enhancement of measurement sensitivity of up to 50 times that of a comparative single-pass reflective measurement is feasible. The waveguide THz-TDS technique also appears to be ideal for the THz (far-infrared) study of precious or hazardous gases, since suitable spectra should be possible with nanogram quantities of material.

APPENDIX A: FIELDS IN THE WAVEGUIDE

To clarify the notation used in this paper and to facilitate comparison with the many different treatments in the literature, we present the formulation used for our calculations of the waveguide coupling and propagation discussed in the main body of this paper. Here, we define the propagating electric (**E**) and magnetic (**H**) fields of the wave in the form

$$\mathbf{E} = \mathbf{E}_0(x, y)\exp(i\omega t - \gamma z),$$
$$\mathbf{H} = \mathbf{H}_0(x, y)\exp(i\omega t - \gamma z). \tag{A1}$$

The complex propagation constant γ can be defined in terms of the real wave propagation constant β and attenuation constant α by

$$\gamma = \alpha + i\beta. \tag{A2}$$

It is convenient to introduce the waveguide and cutoff wavelengths λ_g and λ_c, respectively, through

$$\beta = \frac{2\pi}{\lambda_g} = \frac{2\pi}{\lambda}\left[1 - \left(\frac{\lambda}{\lambda_c}\right)^2\right]^{1/2}, \tag{A3}$$

where λ is the wavelength in the dielectric medium filling the guide, with index of refraction n_d.

We separate the electric and magnetic fields of the propagating wave into transverse and longitudinal components $\mathbf{E}_t$, $\mathbf{H}_t$ and E_z, H_z, respectively. The solutions of Eqs. (A1) that satisfy the boundary conditions comprise the transverse electric (TE) modes, with $E_z = 0$, and the transverse magnetic (TM) modes, with $H_z = 0$. The transverse components of **E** and **H** are related as[12]

$$Z^{\mathrm{TE}}\mathbf{H}_t^{\mathrm{TE}} = \mathbf{k} \times \mathbf{E}_t^{\mathrm{TE}}, \qquad Z^{\mathrm{TE}} = \frac{Z_0}{n_d}\frac{\lambda_g}{\lambda} \text{ for TE},$$
$$Z^{\mathrm{TM}}\mathbf{H}_t^{\mathrm{TM}} = \mathbf{k} \times \mathbf{E}_t^{\mathrm{TM}}, \qquad Z^{\mathrm{TM}} = \frac{Z_0}{n_d}\frac{\lambda}{\lambda_g} \text{ for TM}, \tag{A4}$$

which defines the characteristic impedance of the two types of solutions, where $Z_0 = \sqrt{\mu_0/\epsilon_0}$ is the impedance of the vacuum **k** is the unit vector in the longitudinal (z) direction. The modes are normalized according to

$$\int\!\!\int_S |\mathbf{E}_{tp}|^2 \mathrm{d}S = Z^2 \int\!\!\int_S |\mathbf{H}_{tp}|^2 \mathrm{d}S$$
$$= Z \int\!\!\int_S \mathbf{k} \cdot (\mathbf{E}_{tp} \times \mathbf{H}_{tp}^*)\mathrm{d}S = 1. \tag{A5}$$

There are an infinite number of solutions of the wave equation, each of type TE or TM, corresponding to a particular cutoff wavelength. In the general case, each TE or TM mode can be identified by an integer number p. In practical examples, such as rectangular and circular guides, p refers to a couple of identifying integers: $p \equiv (m, n)$. However, for conciseness we often use the notation p to also include the distinction between TE and TM modes.

The TE and TM modes form a complete and orthogonal basis set for describing the electromagnetic fields within the waveguide.[12,13] We can therefore determine a unique expansion of the incoming electromagnetic field in terms of the normal modes. Each mode propagates freely in the guide, without interacting with the other modes, with a constant cross section, and with the complex propagation constant γ_p responsible for the absorption and the dispersion of the mode. Assuming that the amplitude of the transverse electric field for the pth mode is $A_p\mathbf{E}_{tp}$ for the wave propagating in the $+z$ direction and $B_p\mathbf{E}_{tp}$ for that in the $-z$ direction, the field **E** of the propagating wave in the waveguide is given by

$$\mathbf{E} = \exp(i\omega t)\sum_p \mathbf{E}_{tp}$$
$$\times [A_p \exp(-\gamma_p \cdot z) + B_p \exp(\gamma_p \cdot z)]$$
$$+ \mathbf{k}E_{zp}[A_p \exp(-\gamma_p \cdot z) - B_p \exp(\gamma_p \cdot z)]. \tag{A6}$$

The amplitudes A_p and B_p of each mode are obtained by projection of the transverse components of the incoming electromagnetic field over the transverse pattern of the modes[12,13]:

$$A_p + B_p = \int\!\!\int_S (\mathbf{E}_t \cdot \mathbf{E}_{tp}^*)\mathrm{d}S,$$
$$A_p - B_p = Z_p \int\!\!\int_S (\mathbf{H}_t \cdot \mathbf{H}_{tp}^*)\mathrm{d}S, \tag{A7}$$

where S denotes an integration over the waveguide cross section. We can now analyze separately the propagation of the modes. Simple expressions for the phase velocity v_ϕ and the group velocity v_g of a particular mode in the absence of dispersion of the dielectric medium in the guide are given by

$$v_\phi = \frac{v}{\left[1 - \left(\frac{\lambda}{\lambda_c}\right)^2\right]^{1/2}}, \qquad v_g = v\left[1 - \left(\frac{\lambda}{\lambda_c}\right)^2\right]^{1/2} \tag{A8}$$

with $v = 1/\sqrt{\epsilon\mu}$. Equations (A8) lead to the simple relation $v_\phi v_g = v^2$, for which, in an empty guide, v_ϕ is greater than c, while v_g is naturally less than c. The phase and group velocities for rectangular and circular waveguides are presented below in Figs. 11(b) and 13(b), respectively.

At the input or the output of the waveguide, the change in impedance between free space and the guide results in reflections. The amplitude reflection and transmission coefficients are defined by $r = B/(A + B)$ and $t = A/(A + B)$. The amplitude and power reflection coefficients at the input, r_{in} and R_{in}, and at the output, r_{out} and R_{out}, for the TE and TM modes are given by[13]

$$r_{\mathrm{in}}(\omega) = -r_{\mathrm{out}}(\omega) = \frac{Z(\omega) - Z_0}{Z_0 + Z(\omega)},$$

$$R_{\mathrm{in}} = R_{\mathrm{out}} = |r_{\mathrm{in}}|^2 = |r_{\mathrm{out}}|^2, \tag{A9}$$

where $Z(\omega)$ refers to Z_p^{TE} or Z_p^{TM} as defined in Eqs. (A4) for the TE and TM modes, respectively. The amplitude and power transmission coefficients are also given by[13]

$$t_{\mathrm{in}}(\omega) = \frac{2Z(\omega)}{Z_0 + Z(\omega)}, \qquad t_{\mathrm{out}}(\omega) = \frac{2Z_0}{Z_0 + Z(\omega)},$$

$$T_{\mathrm{in}} = \frac{Z_0}{Z(\omega)} t_{\mathrm{in}}^2, \qquad T_{\mathrm{out}} = \frac{Z(\omega)}{Z_0} t_{\mathrm{out}}^2. \tag{A10}$$

APPENDIX B: RECTANGULAR AND CIRCULAR WAVEGUIDES

The analytic expressions for the modes of rectangular and circular metallic hollow waveguides can be found in Marcuvitz.[11] The electric field patterns for the dominant three modes in a rectangular guide for a linearly polarized, plane-wave Gaussian input beam are presented in Fig. 10. For the rectangular waveguide with horizontal and vertical dimensions $a \times b$, the cutoff wavelength is the same for both the TE_{mn} and TM_{mn} modes and is determined by the two integers m and n:

$$\lambda_c = \frac{1}{\left[\left(\dfrac{m}{2a}\right)^2 + \left(\dfrac{n}{2b}\right)^2\right]^{1/2}}. \tag{B1}$$

However, the characteristic impedances of the TE and TM modes are different and are given by

$$Z^{\mathrm{TE}} = \frac{Z_0}{n_d} \Big/ \left[1 - \left(\frac{\lambda}{\lambda_c}\right)^2\right]^{1/2},$$

$$Z^{\mathrm{TM}} = \frac{Z_0}{n_d}\left[1 - \left(\frac{\lambda}{\lambda_c}\right)^2\right]^{1/2}, \tag{B2}$$

where n_d is the refractive index of the bulk medium in the waveguide, and λ is the wavelength in the bulk medium.

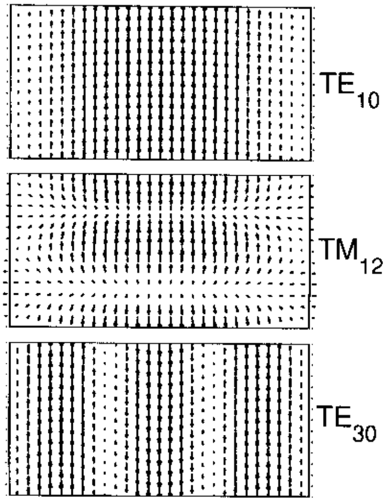

Fig. 10. Electric field patterns of the dominant three modes in a rectangular waveguide.

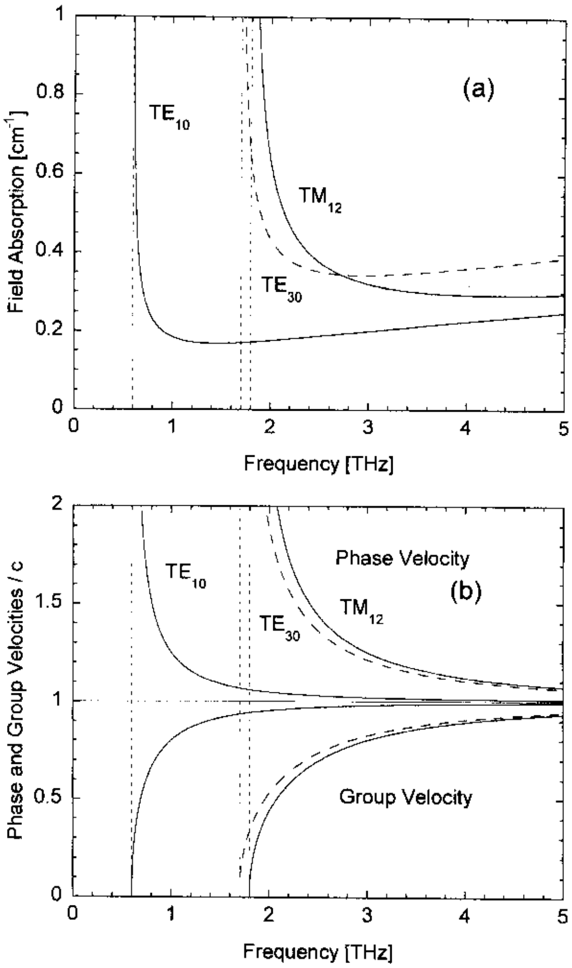

Fig. 11. (a) Field absorption and (b) phase and group velocities for the dominant three modes in the air-filled 250-μm $\times$ 125-μm rectangular brass waveguide.

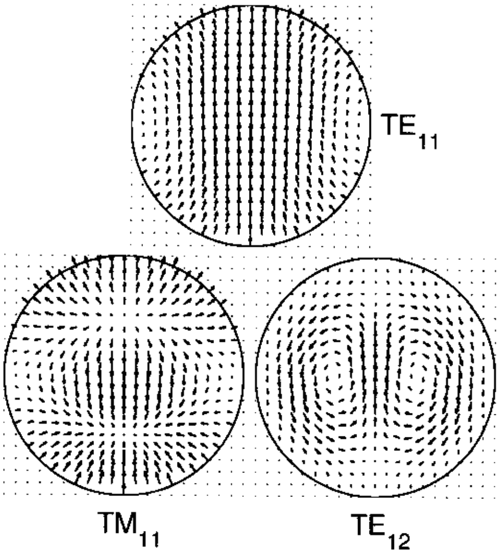

Fig. 12. Electric field patterns of the dominant three modes in a circular waveguide.

The absorption coefficients of the TE_{mn} and TM_{mn} modes for a rectangular waveguide that are due to the finite conductivity of the metal are given by Marcuvitz[11] (Eq. 9, page 60, and Eq. 4, page 57). The absorption and the phase and group velocities of the dominant three modes for a 250-μm × 125-μm brass waveguide are presented in Figs. 11(a) and 11(b), respectively.

For a circular waveguide, the cutoff frequencies of the TE_{mn} and TM_{mn} modes are determined by the nth roots of the mth-order Bessel function and of the derivative of the mth-order Bessel function.[11] The characteristic impedances are the same as those for the rectangular guide [Eqs. (A4)]. The electric field patterns of the dominant three modes in a circular guide, for a linearly polarized, plane-wave Gaussian input beam, are presented in Fig. 12.

The absorption of a circular waveguide that is due to the finite conductivity of the metal has been calculated by using the expression given by Marcuvitz[11] (Eq. 25, page 70, and Eq. 21, page 67). The absorption coefficient and the phase and group velocities of the dominant three modes for a 240-μm-diameter stainless-steel waveguide are presented in Figs. 13(a) and 13(b), respectively.

APPENDIX C: ABSORPTION FROM A LAYER WITH THE WAVEGUIDE

We consider the absorption of waveguides partially filled with a thin dielectric layer by using Poynting's theorem, which states the conservation of electromagnetic energy as[13]

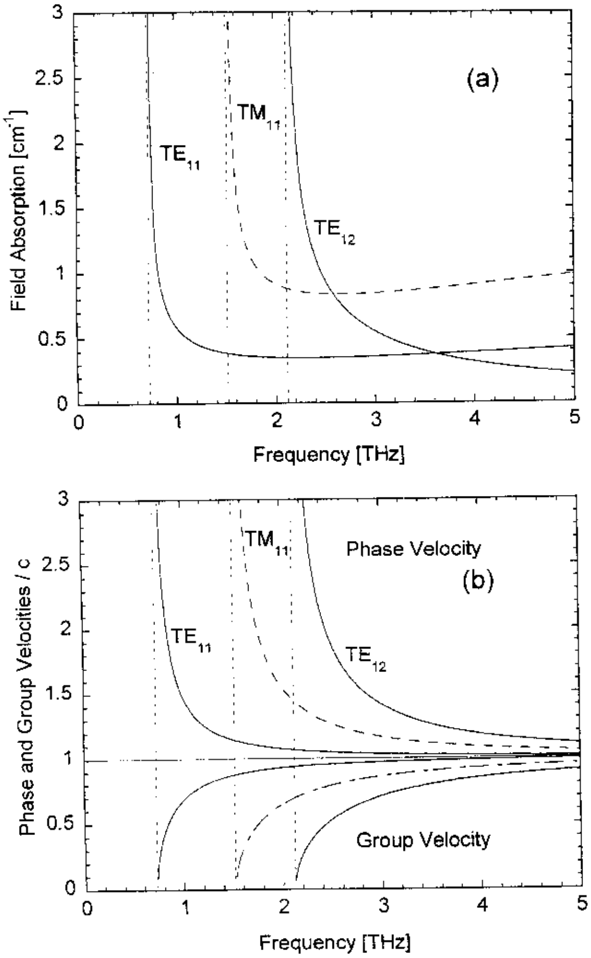

Fig. 13. (a) Field absorption and (b) phase and group velocities for the dominant three modes in a 240-μm-diameter stainless-steel waveguide.

$$\frac{\partial W}{\partial z} + \frac{1}{v_g}\frac{\partial W}{\partial t} = -\frac{\omega}{Q}\frac{W}{v_g}, \qquad \text{(C1)}$$

where W is the total energy per unit length, defined by integration of the energy density over the cross section of the waveguide, v_g is the group velocity, and Q is defined by analogy to oscillating circuits. To explain Q, we can rewrite Eq. (C1) by using the reduced time $t^* = t - z/v_g$ to obtain

$$\frac{\partial W}{\partial t^*} = -\frac{\omega}{Q} W. \qquad \text{(C2)}$$

The factor Q corresponds to the energy loss in an elementary cell traveling in the guide with the same velocity v_g as the flow of energy, so that the energy in the cell decreases as $\exp(-\omega t^*/Q)$. If W_l and W_g are defined as the energy per unit length in a cross section of the layer and the empty remaining space of the waveguide, respectively, the total energy W is given by $W = W_l + W_g$. We write the conservation of energy, for both the layer and the empty space, as

$$v_g \frac{\partial W_l}{\partial z} = -\frac{\omega}{Q_{g,l}} W_l - r_{12} W_l + r_{21} W_g, \qquad \text{(C3)}$$

$$v_g \frac{\partial W_g}{\partial z} = r_{12} W_l - r_{21} W_g, \qquad \text{(C4)}$$

where r_{12} and r_{21} are the energy-transfer rates between the layer and the empty space and $Q_{g,l}$ is the energy loss in the layer within the waveguide. Summing Eqs. (C3) and (C4) and defining the filling factor f such that $W_l = fW$, we obtain

$$v_g \frac{\partial W}{\partial z} = -\frac{\omega}{Q_{g,l}} W_l = -\frac{\omega f}{Q_{g,l}} W = -2\alpha_{g,l} v_g W. \qquad \text{(C5)}$$

In Eq. (C5) we have defined the absorption constant $\alpha_{g,l}$ of the waveguide so that W decreases as $\exp(-2\alpha_{g,l} z)$. We also define the bulk absorption for the material in the layer by α_l so that the energy in the bulk of the material decreases as $\exp(-2\alpha_l z)$. Applying Poynting's theorem to the bulk of the material constituting the layer, where the energy flow in the bulk material travels with the velocity v_l, one obtains a relationship between Q_l and α_l:

$$v_l \frac{\partial W}{\partial z} = -\frac{\omega}{Q_l} W = -2\alpha_l v_l W. \qquad \text{(C6)}$$

Assuming that $Q_l = Q_{g,l}$ then leads to the relationship

$$\alpha_{g,l} = f\alpha_l \frac{v_l}{v_g}. \qquad \text{(C7)}$$

We have calculated expressions for the filling factor of a thin dielectric layer on the surface of rectangular and circular air-filled waveguides. For a rectangular guide of dimensions $a \times b$ with a dielectric layer of thickness Δl and refractive index n_l on the side of dimension a, the filling factors f_{mn} and g_{mn} for the TE_{mn} and TM_{mn} modes, respectively, are

$$f_{mn} = \frac{W_{l,\mathrm{TE}}}{W_{\mathrm{TE}}} = \frac{\delta_m \delta_n}{n_l^2}\frac{m^2\lambda_c^2}{8a^2}\frac{\Delta l}{b},$$

$$g_{mn} = \frac{W_{l,\mathrm{TM}}}{W_{\mathrm{TM}}} = \frac{1}{n_l^2}\frac{n^2\lambda_c^2}{2b^2}\frac{\Delta l}{b}, \tag{C8}$$

where

$$\delta_p = \begin{cases} 1 & \text{if } p = 0 \\ 2 & \text{if } p \neq 0 \end{cases} \quad \text{with } p = m \text{ or } n. \tag{C9}$$

For example, the filling factor of the TE_{10} mode is

$$f_{10} = \frac{\Delta l}{b n_l^2}, \tag{C10}$$

corresponding to the ratio of the cross-section area of the layer to the total cross-section area of the guide, multiplied by the reciprocal of the squared index of the layer, which is proportional to the energy density in the layer.

For an air-filled circular guide of radius a and a layer of thickness Δl at the surface of the guide, consideration of the energy densities in the guide and the layer leads to the TE and TM filling factors, f_{mn} and g_{mn}, respectively;

$$f_{mn} = \frac{1}{n_l^2}\frac{\pi\delta_m}{\dfrac{4\pi^2a^2}{m^2\lambda_c^2} - 1}\frac{\Delta l}{a},$$

$$g_{mn} = \frac{\delta_m}{n_l^2}\left[\frac{J_m'(2\pi a/\lambda_c)}{J_{m+1}(2\pi a/\lambda_c)}\right]^2\frac{\Delta l}{a}. \tag{C11}$$

ACKNOWLEDGMENTS

We acknowledge careful reading of this manuscript and many helpful and stimulating suggestions by R. Alan Cheville, John O'Hara, and Jiang-Quan Zhang. Rajind Mendis was especially helpful through his many discussions of the waveguide solutions of Maxwell's equations and in particular for his help in clarifying the boundary conditions for the dielectric layer. The work was partially supported by the National Science Foundation and the U.S. Army Research Office.

Address correspondence to D. Grischkowsky at the location on the title page or by phone, 405-744-6622; fax, 405-744-9198; or e-mail, grischd@master.ceat.okstate.edu.

*Present address, Laboratoire d'Optique Quantique, CNRS, Ecole Polytechnique, 91128 Palaiseau cédex, France.

†Present address, Department of Physics and Applied Physics, University of Strathclyde, Glasgow, UK.

‡Present address, Imation, Oakdale, Minnesota 55128.

REFERENCES

1. M. van Exter and D. Grischkowsky, "Characterization of an optoelectronic terahertz beam system," IEEE Trans. Microwave Theory Tech. **38**, 1684–1691 (1990).
2. D. Grischkowsky, S. Keiding, M. van Exter, and Ch. Fattinger, "Far-infrared time-domain spectroscopy with terahertz beams of dielectrics and semiconductors," J. Opt. Soc. Am. B **7**, 2006–2015 (1990).
3. R. W. McGowan, G. Gallot, and D. Grischkowsky, "Propagation of ultra-wideband, short pulses of THz radiation through sub-mm diameter circular waveguides," Opt. Lett. **24**, 1431–1433 (1999).
4. A. Nahata and T. F. Heinz, "Reshaping of freely propagating terahertz pulses by diffraction," IEEE J. Sel. Top. Quantum Electron. **2**, 701–708 (1996).
5. J. Bromage, S. Radic, G. P. Agrawal, C. R. Stroud, Jr., P. M. Fauchet, and R. Sobolewsky, "Spatiotemporal shaping of half-cycle terahertz pulses by diffraction through conductive apertures of finite thickness," J. Opt. Soc. Am. B **15**, 1399–1405 (1998).
6. C. Winnewisser, F. Lewen, J. Weinzierl, and H. Helm, "Transmission features of frequency-selective components in the far-infrared determined by terahertz time-domain spectroscopy," Appl. Opt. **38**, 3961–3967 (1999).
7. J. W. Digby, C. E. Collins, B. M. Towlson, L. S. Karatzas, G. M. Parkhurst, J. M. Chamberlain, J. W. Bowen, R. D. Pollard, R. E. Miles, D. P. Steenson, D. A. Brown, and N. J. Cronin, "Integrated micromachined antenna for 200 GHz operation," in *International Microwave Symposium Digest* (Institute of Electrical and Electronics Engineers, New York, 1997), pp. 561–654.
8. J. Lesurf, *Millimeter-Wave Optics, Devices and Systems* (Hilger, Bristol, UK, 1990).
9. A. Taflove, *Computational Electrodynamics: The Finite-Difference Time-Domain Method* (Artech House, Norwood, Mass., 1995).
10. P. A. Rizzi, *Microwave Engineering, Passive Circuits* (Prentice-Hall, Englewood Cliffs, N.J., 1988).
11. N. Marcuvitz, *Waveguide Handbook* (Peregrinus, London, 1993).
12. J. C. Slater, "Microwave electronics," Rev. Mod. Phys. **18**, 441–512 (1946).
13. J. C. Slater, *Microwave Electronics* (Van Nostrand, New York, 1950).